ELSEVIER

Contents lists available at ScienceDirect

Computational Materials Science

journal homepage: www.elsevier.com/locate/commatsci



Full length article

pySSpredict: A python-based solid-solution strength prediction toolkit for complex concentrated alloys

Dongsheng Wen*, Michael S. Titus

School of Materials Engineering, Purdue University, 701 West Stadium Ave, West Lafayette, IN 47907, USA



ARTICLE INFO

Dataset link: https://github.com/Dongsheng-Wen/pySSpredict, https://nanohub.org/tools/pysspredict

Keywords:
Solid-solution strengthening
Complex concentrated alloys
Yield strengths
Dislocations
High-throughput calculations

ABSTRACT

The emergence of solid solution high entropy alloys (HEAs) and complex concentrated alloys (CCAs) offers opportunities to design novel alloys with tailored strength and ductility. The growing community of integrated-computational materials engineering (ICME) can benefit from implementing state-of-the-art solid-solution strengthening models to alloy design practices. This paper introduces *pySSpredict*, an open-source python-based toolkit that automates high-throughput calculations of solid-solution strengths of CCAs and thermodynamic properties. We present the functions of the pySSpredict code: (1) automating high-throughput calculations of strength for CCAs, (2) managing the data of thermodynamic calculations from databases or other software, and (3) visualizing and filtering the data to identify candidate alloys. The toolkit implements the latest theoretical edge dislocation model for face-centered cubic (FCC), and edge/screw dislocation models for body-centered cubic (BCC) alloys. The pySSpredict code is hosted on GitHub and deployed on nanoHUB for demonstrations.

1. Introduction

Achieving a balance of high strength and high toughness engineering structural alloys has always been a challenging goal in traditional materials discovery [1]. The solid-solution phase of many metallic alloys maintains a good balance of strength and ductility and has been the focus of structural alloys under extreme working environments. Example of such use include Co-rich solid solutions which has been employed to strengthen the metallic matrix in powder metallurgy hard metal alloys [2,3] and the matrix phase in superalloys [4]. The face-centered cubic (FCC) NiCoCr has been known for its exceptional strength-ductility combination at elevated temperatures due to the strong solute-dislocation interactions [5]. The body-centered cubic (BCC) MoNbTaVW alloy has high dislocation energy barrier due to the atomic misfit contributed by the alloying elements [6]. The nonequiatomic FeMnCoCr alloys exhibit remarkable plasticity due to the FCC-HCP phase transformation induced by plastic strains and composition modifications, which can be attributed to their low-to-medium stacking fault energies [7].

The emergence of solid solution high entropy alloys (HEAs) [8–10] and complex concentrated alloys (CCAs) [11] offers opportunities to design novel alloys with good strength and ductility. The concept of CCAs emphasizes that an alloy is based on more than one principal element (usually more than three), which tremendously expands the alloying systems and the composition space of searching at elevated

temperatures. A large number of studies have been focused on designing novel CCAs with extraordinary yield strengths [11]. These related studies have demonstrated that the traditional trial-and-error experimental processes must be replaced by the more rigorous integrated computational materials engineering (ICME) methods, which require both high-throughput experiments and computations [12,13].

The strength of solid-solution CCAs relies on the presence and interactions of solute atoms that accumulate near the dislocations and hinder dislocation motion [14]. Historic Labusch-type models and Suzuki models for solid-solution strengthening have been developed and extended to CCAs in recent years [6,15–17]. These recent theoretical developments can now be utilized for high-throughput calculations to optimize alloy strength [6,12,16,18–21]. The full potentials of the models within the ICME can be achieved with the combination of (1) a program that automates the high-throughput calculations of strengths for CCAs, (2) an interface that manage the thermodynamic calculations with available database or other software, and (3) a simple visualization program that helps identify candidate alloys.

Despite the efforts made to tackle the vast composition space of CCAs [6,12,18,20,21], the community of metallurgists will benefit from an open-source and automated toolkit for materials discovery. This paper introduces pySSpredict, a python-based toolkit that automates the high-throughput calculations of solid-solution strengths of CCAs

E-mail address: wen94@purdue.edu (D. Wen).

Corresponding author.

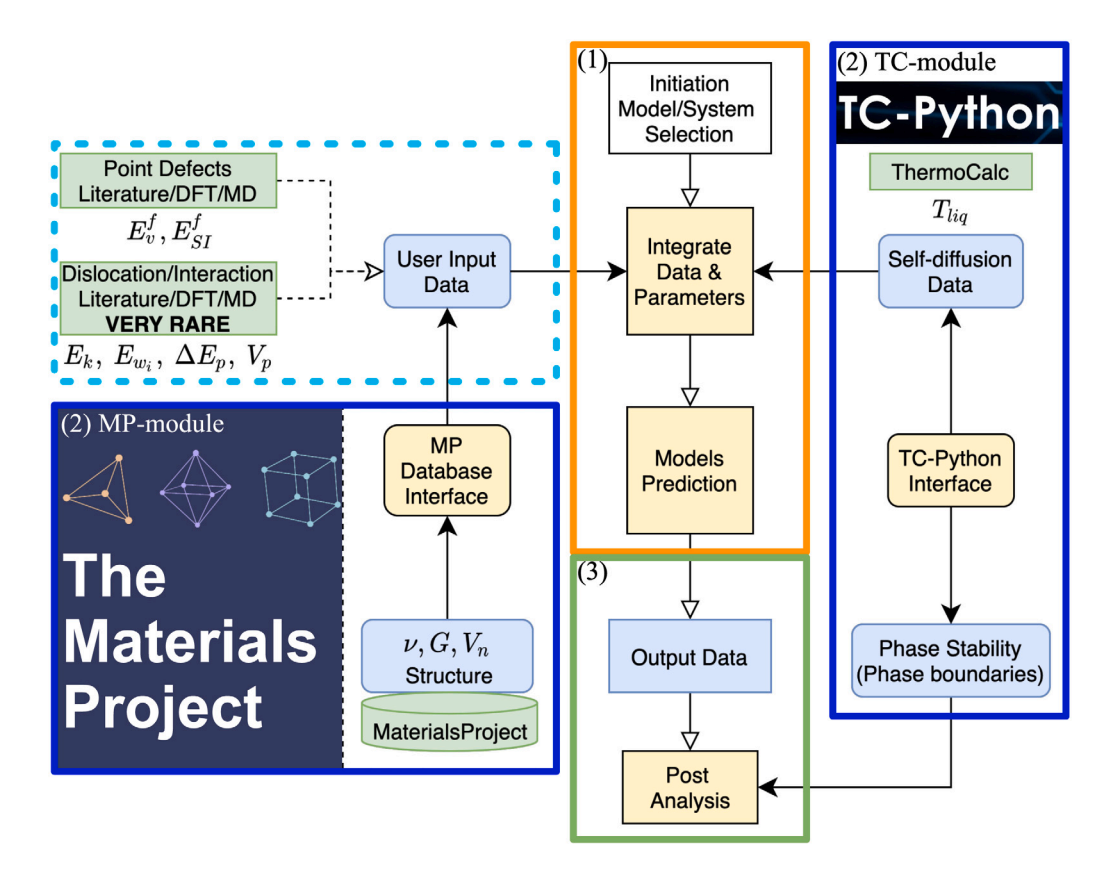


Fig. 1. The workflow of pySSpredict shows three major functions: (1) data integration and calculation (orange box), (2) MP-interface and TC-python interface (blue boxes), and (3) data visualization (green box).

and thermodynamic properties. The pySSpredict code is hosted on GitHub [22] and deployed on nanoHUB [23] for demonstrations.

2. Methods

The general workflow of pySSpredict consists of three parts, see Fig. 1. Part 1: The user can initiate a project by specifying the alloy system and solid-solution models, setting up the input data and parameters, and then making predictions and collecting data for analysis, see the orange box in Fig. 1. The data is structured using pandas.DataFrame [24], which can be easily visualized and written to JSON or CSV files. Part 2: This module includes two interfaces for materials data. First, DFT data, such as elastic constants and lattice parameters, can be directly fetched from the Materials Project [25,26] using the MP-interface. Second, thermodynamic phase predictions and liquidus temperatures are required for identifying single-phase regions, which can be calculated using the TC-Python interface within the Thermo-Calc software [27]. The TC-python interface can perform highthroughput single-point equilibrium calculations by looping over userdefined compositions and temperatures. Material data such as point defect energies and solute-dislocation interaction energies are rare and must be determined from more sophisticated first-principles calculations [28-34]. Part 3: The predicted data can be organized/visualized for post analysis using the built-in functions (see green box in Fig. 1).

2.1. Solid-solution strengthening models

The pySSpredict tool implements four recently developed solidsolution strengthening models for CCAs: (1) the FCC edge dislocation model [15], (2) the BCC edge dislocation model [6], (3) the BCC screw dislocation Curtin model [16], and (4) the BCC screw dislocation Suzuki model [30]. The screw dislocations are not implemented for FCC, which is due to the difficulties in determining meaningful dislocation parameters for accurate high-throughput computations. The stress field of screw dislocations is not likely to interact with the hydrostatic stresses around a solute atom in the gliding direction [19]. Ma et al. have shown that the interaction energy between the solute and screw dislocations are about half of those between the solute and edge dislocations, and the core of the screw dislocation is less dissociated than the edge dislocation [35]. Multi-component FCC systems usually exhibit medium stacking fault energies and result in partially-dissociated edge dislocation glide rather than perfect dislocation glide [19]. For the implemented models, the symbols and definitions of the important input properties are provided in Table 1. The symbols, definitions, and default values of the adjustable parameters in the models are tabulated in Table 2.

2.1.1. Edge dislocation models for FCC and BCC solid solutions

The edge dislocation models for FCC and BCC structures are similar regarding the general frameworks and formulations [6,15]. Therefore, the key formulae, inputs, and outputs of the two models will be summarized below. The full theories and reduced models are well developed in the articles [6,15]. The key equations implemented in the software are:

$$\tau_{y0} = 0.051 \alpha^{-1/3} \mu \left(\frac{1+\nu}{1-\nu} \right)^{4/3} f_1 \left[\frac{\sum_n c_n \Delta V_n^2}{\bar{b}^6} \right]^{2/3}$$
 (FCC or BCC) (1a)

$$\Delta E_b = 0.274 \alpha^{1/3} \mu \bar{b}^3 \left(\frac{1+\nu}{1-\nu}\right)^{2/3} f_2 \left[\frac{\sum_n c_n \Delta V_n^2}{\bar{b}^6}\right]^{1/3}$$
 (FCC or BCC) (1b)

$$\tau_{y}(T,\dot{\epsilon}) = \tau_{y0} \left[1 - \left(\frac{kT}{\Delta E_{b}} ln \frac{\dot{\epsilon_{0}}}{\dot{\epsilon}} \right)^{2/3} \right] (if \frac{\tau_{y}}{\tau_{y0}} > 0.5)$$
 (1c)

Definitions and input entries of input properties for different models. Models: (1) FCC edge dislocation model, (2) BCC edge dislocation model, (3) BCC screw dislocation Curtin model, and (4) BCC screw dislocation Suzuki model.

Symbol	Definition	Unit	Software entry	Model
a, b	Lattice parameter and Burgers vector	Å	a, b	1, 2, 3, 4
V_n	Elemental atomic volume	$\mathring{\mathbf{A}}^3$	V_n	1, 2, 3, 4
$ar{V}$	Averaged atomic volume	$\mathring{\mathbf{A}}^3$	_	1, 2, 3, 4
ΔV_n	Misfit volume of element	$\mathring{\mathbf{A}}^3$	-	1, 2
ν	Poisson ratio	_	nu	1, 2, 3, 4
μ	Shear modulus	GPa	G	1, 2, 3, 4
C_{ii}	Stiffness matrix (6 × 6)	GPa	Cij	1, 2, 3, 4
c_n	Atomic concentration	at.%	set_comp()	1, 2, 3, 4
T	Temperature	K	set_temp()	1, 2, 3, 4
Ė	Strain rate	/s	set_strain_r()	1, 2, 3, 4
$\dot{\epsilon_0}$	Reference strain rate	/s	10^{4}	1, 2
$\Delta ilde{E}_p$	Characteristic energy fluctuation due to solute–dislocation interaction	eV	Delta_E_p	3
$\Delta V_{_{D}}$	Peierls barrier of screw dislocation per Burbers vector	eV/b	Delta_V_p	3
E_k	Kink formation energy for screw dislocation	eV	E_k	3
E_v^f	Formation energy of vacancy	eV	E_f_v	3, 4
E_{si}^f	Formation energy of self-interstitial	eV	E_f_si	3, 4
E_{wi}^{si}	Solute-screw dislocation interaction energy	eV	E_w_i	4
T_l	Liquidus temperature	K	set_T_1()	4

$$\tau_{y}(T,\dot{\varepsilon}) = \tau_{y0} exp \left[-1.754 \frac{kT}{\Delta E_{h}} ln \frac{\dot{\epsilon}_{0}}{\dot{\varepsilon}} \right] (if \frac{\tau_{y}}{\tau_{y0}} < 0.5)$$
 (1d)

in which τ_{v0} is the zero-K yield stress, ΔE_b is the energy barrier of edge dislocations, and $\tau_v(T,\dot{\varepsilon})$ is the yield stress at finite temperatures (T) and strain rates $((\dot{\varepsilon}))$ conditions. Solutes with various atomic sizes contribute to the stress and the energy barrier mainly through the atomic misfits (ΔV_n) and alloy compositions c_n [15]. Within the elastic region, the stress field of the dislocation is contributed by the shear modulus (μ) , Poisson ratio (ν) , the line tension parameter (α) , and the dimensionless structure coefficients f_1 and f_2 [15]. At finite temperatures and strain rates, the activated dislocations can exhibit the low-temperature ($\frac{\tau_y}{\tau_{y0}}$ < 0.5) single bow out and the high-temperature $(\frac{\tau_y}{}$ < 0.5) multi-scale bow out configurations, resulting in slightly different stress-temperature relationships [15].

2.1.2. BCC screw dislocation Curtin model

Maresca and Curtin derived the solid-solution strength of BCC alloys by considering the solute-screw dislocation interactions [16]. The key equations implemented in the software are:

$$\tau(\dot{\epsilon},T) = \tau_{xk}(\dot{\epsilon},T) + min[\tau_k(\dot{\epsilon},T),\tau_P(\dot{\epsilon},T)] \tag{2a}$$

$$\tau_{xk}(\dot{e}, T) = max \left[\frac{\pi E_{si}^f}{ab \xi_{si}} \left(1 - \left(\frac{\Delta H}{E_{si}^f} \right)^{2/3} \right), \quad \frac{\pi E_v^f}{ab \xi_v} \left(1 - \left(\frac{\Delta H}{E_v^f} \right)^{2/3} \right) \right] \quad \text{(2b)}$$

$$\Delta H = kT \ln \frac{\dot{\epsilon}_0}{\dot{\epsilon}}, \quad \xi_{si} = 15\xi_c, \quad \xi_v = 7.5\xi_c, \quad \xi_c = (1.083E_k/\Delta \tilde{E}_p)^2 b$$
 (2c)

$$\Delta H = kT \ln \frac{\dot{\epsilon_0}}{\dot{\epsilon}}, \quad \xi_{si} = 15\xi_c, \quad \xi_v = 7.5\xi_c, \quad \xi_c = (1.083E_k/\Delta \tilde{E}_p)^2 b$$

$$\tau_k(\dot{\epsilon}, T) = \tau_b + \frac{(\tau_{k,0} - \tau_b)}{exp\left[\frac{0.89\Delta H}{\Delta E_{k,0}} + 0.5\left(\frac{\Delta H}{\Delta E_{k,0}}\right)^{0.25} + 0.6\right] - 1}$$

$$(if \frac{(\tau - \tau_b)}{(\tau_{k,0} - \tau_b)} > \frac{1}{(5.75\xi_c/w_k + 1)})$$
 (2d)

$$\tau_k(\dot{\epsilon},T) = \tau_b - \frac{(\tau_{k,0} - \tau_b) w_k \Delta H}{5.75 \xi_c \Delta E_{k,0}} \quad (if \ \frac{(\tau - \tau_b)}{(\tau_{k,0} - \tau_b)} < \frac{1}{(5.75 \xi_c / w_k + 1)})$$

$$\tau_P(\dot{\epsilon}, T) = \tau_{P,0} [1 - (\Delta H / \Delta E_{b,P})^{2/3}]$$
 (2f)

$$\tau_{p}(\varepsilon, I) = \tau_{P,0}[1 - (\Delta H/\Delta E_{b,P})^{T}]$$

$$\tau_{b} = \frac{1.08E_{k}}{ab\xi_{c}}, \quad \Delta E_{k,0} = 1.37\Delta \widetilde{E}_{p}\sqrt{\frac{w_{k}}{b}}, \quad \Delta E_{b,P} = \frac{(10\Delta V_{p}\xi_{c} + 0.7E_{k})^{3}}{(20\Delta V_{p}\xi_{c} + 0.7E_{k})^{2}}$$
(2g)

$$\tau_{P,0} = \frac{\pi \Delta V_P}{ba} + \frac{0.44 E_k}{ba \xi_c} \left[1 - \frac{5 \Delta V_P \xi_c}{20 \Delta V_p \xi_c + 0.7 E_k} \right]$$
 (2h)

in which the overall stress $(\tau(\dot{\epsilon}, T))$ is contributed by three mechanisms: (1) the cross-kink mechanism $\tau_{xk}(\dot{\epsilon},T)$, (2) the kink glide mechanism $\tau_k(\dot{\epsilon},T)$, and (3) the Peierls mechanism $\tau_P(\dot{\epsilon},T)$. Maresca et al. found that the kink glide and Peierls modes are competing mechanisms that the screw dislocation can move through kink segments or the entire dislocation line, depending on the solute-dislocation interactions at equilibrium configurations [16]. The cross-kink mechanism stems from the dislocations pinned by vacancies or self-interstitials with different formation energies. Different contributions can be calculated individually for analysis and materials design. The inputs and main parameters are given in Tables 1 and 2.

2.1.3. BCC screw dislocation Suzuki model

The Suzuki model is well-known for predicting the elemental contributions to the overall yield strength of BCC alloys [17]. The recent application of the Suzuki model by Rao et al. considered a hightemperature jog-dragging mode caused by the concentration gradient of vacancies near the jog [30]. The set of equations implemented for this model is summarized below:

$$\tau_{v,i} = \tau_{k,i}(L) + \tau_{j,i}(L); \quad where \quad \partial \tau_{v,i}/\partial L = 0$$
 (3a)

$$\tau_{j,j}(L) = (E_v^f + E_{sj}^f)/4bL$$
 (3b)

$$\tau_{k,i}^4 + S\tau_{k,i} - R = 0 (3c)$$

$$S = \left[\frac{18\kappa^2 E_{ui}^2 c_n kT}{a_D^3 b^4 A_b^2} \right] ln \left[\frac{(5\pi kT)^2 v_0 a_D b}{(\mu b \Delta V)^2 \dot{\epsilon}} \right]$$
(3d)

$$R = \frac{27\kappa^4 E_w i^4 c_n^2}{a_P^4 b^6 A_k^2}$$
 (3e)

$$\Delta V = \frac{3\kappa^2 E_{wi}^2 c_n}{2\tau_k^2 a_p b^2} + \frac{\tau_k^2 a_p^3 b^4 \Lambda_k^2}{6\kappa^2 E_{wi}^2 c_n}$$
(3f)

$$\frac{b}{3Lc_n} = \frac{1}{\sqrt{2\pi}} \int_{\kappa}^{+\infty} exp(-x^2/2) dx$$
 (3g)

$$\tau_y = \left[\sum (\tau_{y,i})^{1/q}\right]^q \tag{3h}$$

$$\tau_{j,i}(L) = \frac{kT}{2Lb^2} ln \left[\frac{\dot{\epsilon}}{2.598\pi\rho D} + \left[1 + \left(\frac{\dot{\epsilon}}{2.598\pi\rho D} \right)^2 \right]^{0.5} \right]$$
 (3i)

$$D = 14v_0b^2 exp(-19.12T_l/T)$$
 (3j)

in which the yield stress contribution from solute-i is controlled by the bowing stress and the kink movements of the screw dislocation. The Suzuki model minimizes stresses from the stress by bowing (τ_i) and

Table 2

Definitions and default values of adjustable parameters for different models. Models: (1) FCC edge dislocation model, (2) BCC edge dislocation model, (3) BCC screw dislocation Curtin model, and (4) BCC screw dislocation Suzuki model.

Symbol	Definition	Unit	Software entry	Default values	Model
Averaging scheme	Set the averaging method for elastic constants. Available methods: Vegard's law and Voigt method.	-	set_averaging_scheme()	default is Vegard's law	1, 2
f_1	Structure coefficient in the athermal stress for dislocation cores.	-	f1	FCC: 0.35, BCC: 0.7844	1, 2
f_2	Structure coefficient in the energy barrier for dislocation cores.	-	f2	FCC: 5.7, BCC: 7.2993	1, 2
α	Dislocation line tension parameter.	-	alpha	0.123	1, 2
$S_{\Delta V_a}$	Fitting parameter for ab initio ΔV_p .	-	Delta_V_p_para	1.0	3
$S_{\Delta ilde{E_n}}^{^p}$	Fitting parameter for ab initio $\Delta \hat{E_p}$.	-	Delta_V_p_para	1.0	3
w_k	Kink width.	b	kink_width	10.0	3, 4
q	Exponent of phenomenological law of stress contributions.	-	tau_i_exponent	1.0	4
ρ	Dislocation density.	$/m^2$	dislocation_density	4×10^{13}	4
$\tilde{ au}_{\kappa}$	Trial τ_{κ} for the stress minimization process.	MPa	tau_kappa	5.0	4
κ̈́	Trial κ for the stress minimization process.	-	trial_kappa	min: 1, max:4	4

the stress by kink (τ_k) on a segment pinned by the interstitial/vacancy dipoles. In this theory, the kink movement involves the solute–kink interactions, and the bowing stress involves the equilibrium dipole length between the vacancy/interstitial dipoles [30]. Eqs. (3) are solved numerically by minimizing Eq. (3a) with respect to κ , the parameter for equilibrium dipole spacing. And the quartic equation of Eq. (3c) can be solved by providing initial values of τ_k . Therefore, initial trial values noted as κ and τ_k , are set for the calculation. At a higher temperature, the onset of the jog-dragging mode can be estimated when the diffusivity of the thermally activated vacancies satisfies ($\sqrt{Dt} > b$ with $t = 0.002/\dot{\epsilon}$) [30]. When jog-dragging is activated, Eq. (3i) replaces Eq. (3b) in the minimization process. And finally, if the formation energies of vacancy and self-interstitial (E_v^f and E_{si}^f) are not provided, the Frank–Read bowing stress model is used for $\tau_{i,i} = \mu b/4L$ [17].

3. Model verification and discussion

The strength of an arbitrary alloy composition can be calculated through the module sspredict.make_prediction and the function single_calc_wrapper. Demonstrations are shown below to introduce the strengthening models with their necessary input properties and parameters. Detailed codes of the calculations and the functions are also published as simulation Jupyter notebooks hosted on nanoHUB [23].

3.1. FCC and BCC edge dislocation

The strengths of the FCC CrMnFeCoNi and the BCC MoNbTaVW equimolar alloys are predicted using the edge dislocation models, and the results match the literature data calculated with the same input data [6,19], see Fig. 2(a) and 2(b). For reproducing the results, the atomic volumes of the elements are tabulated in Table 3. The shear modulus and Poisson ratios for the CrMnFeCoNi are 80 GPa and 0.26, respectively, and the shear modulus and Poisson ratio for the MoNbTaVW are 92 GPa and 0.43, respectively. The experimental strain rate is set to 0.001/s for both predictions. As for the MoNbTaVW alloy, the transition from the single-scale bow out to the multiple-scale bow out can be observed between 800 K and 900 K [6], see Fig. 2(b). This transition was also reported when the full theory was employed [6]. As for the FCC CrMnFeCoNi alloy, however, the transition is not observed in the considered temperature range; the multiple-scale bow out mechanism dominates (see Fig. 2(a) where the red and yellow lines are overlapped). This is because the FCC alloys have relatively lower energy barriers than the BCC alloys, and the dislocations are easier to be thermally activated at lower temperatures to reach the multiple-scale bow out condition [19].

To make useful predictions, reasonable values should be set to the parameters related to the dislocation core structure. For the edge $\frac{1}{2}$

Table 3 Atomic volumes, $V_n(\mathring{A}^3)$, of the CrMnFeCoNi and MoNbTaVW alloys. *Source:* Data obtained from Refs. [6,19].

Cr	Mn	Fe	Co	Ni	Мо	Nb	Ta	V	W
12.27	12.60	12.09	11.12	10.94	15.44	17.65	17.97	14.85	16.07

Input properties of the BCC Nb95Mo5 alloy.

a(Å)	$\Delta \tilde{E}_p$ (eV)	E_k (eV)	E_v^f (eV)	E_{si}^f (eV)	ΔV_P (eV/b)
3.289	0.0488	0.6342	2.989	5.361	0.02

dislocation models, α , f_1 , and f_2 can be changed before the strength calculation. α is the line tension parameter of the edge dislocation with common values between 0.0625 to 0.125 [6,19]. f_1 and f_2 are parameters related to the stress pressure field of the equilibrium dislocation configuration. The values of f_1 and f_2 can vary with the stacking fault energy of the alloys [19], and the default values in Table 2 are obtained from the effective values by fitting the reduced models across different alloys [6].

3.2. BCC screw dislocation — Curtin model

The predicted stresses of the BCC Nb95Mo5 are shown in Fig. 2(c), in which the total yield stresses agree with the data from the original paper using the same input data in Table 4 [16]. The model has three additive mechanisms: the kink-glide mechanism, the cross-kink mechanism, and the Peierls mechanism. The Peierls mechanism dominates when the temperature is below 25 K. From 25 K to 500 K, kink-glide is the dominating mechanism; its strength contribution decreases with increasing temperature, see blue line in Fig. 2(c). The cross-kink mechanism is controlled by either the vacancy or the self-interstitial that they pin the dislocations at different lengthscales [16]. The cross-kink contribution becomes comparable to the kink-glide contribution at 400 K and higher temperatures. As the kink-glide contribution continues to decrease, the cross-kink mechanism is the major strengthening mechanism at higher temperatures.

It should be noted that $\Delta \tilde{E}_p$, ΔV_p , and E_k require extended DFT/MD calculations with larger dislocation supercells [16]. And re-scaled values may be used by fitting the DFT-0K data to the experimental yield strengths [16]. The $S_{\Delta E_p}$ and $S_{\Delta V_p}$ are fitting parameters for $\Delta \tilde{E}_p$ and ΔV_p , respectively. In Maresca and Curtin's study, for the Nb-Mo system, the $\Delta \tilde{E}_p$ values calculated by MD simulations using Zhou's potential are rescaled with a factor of 0.79 to match the experimentally measured yield stress [16]. The ΔV_p for this Nb-Mo system was fitted to the experimental yield stress at low temperatures where the Peierls mechanism is expected to dominate [16]. As mentioned in their study,

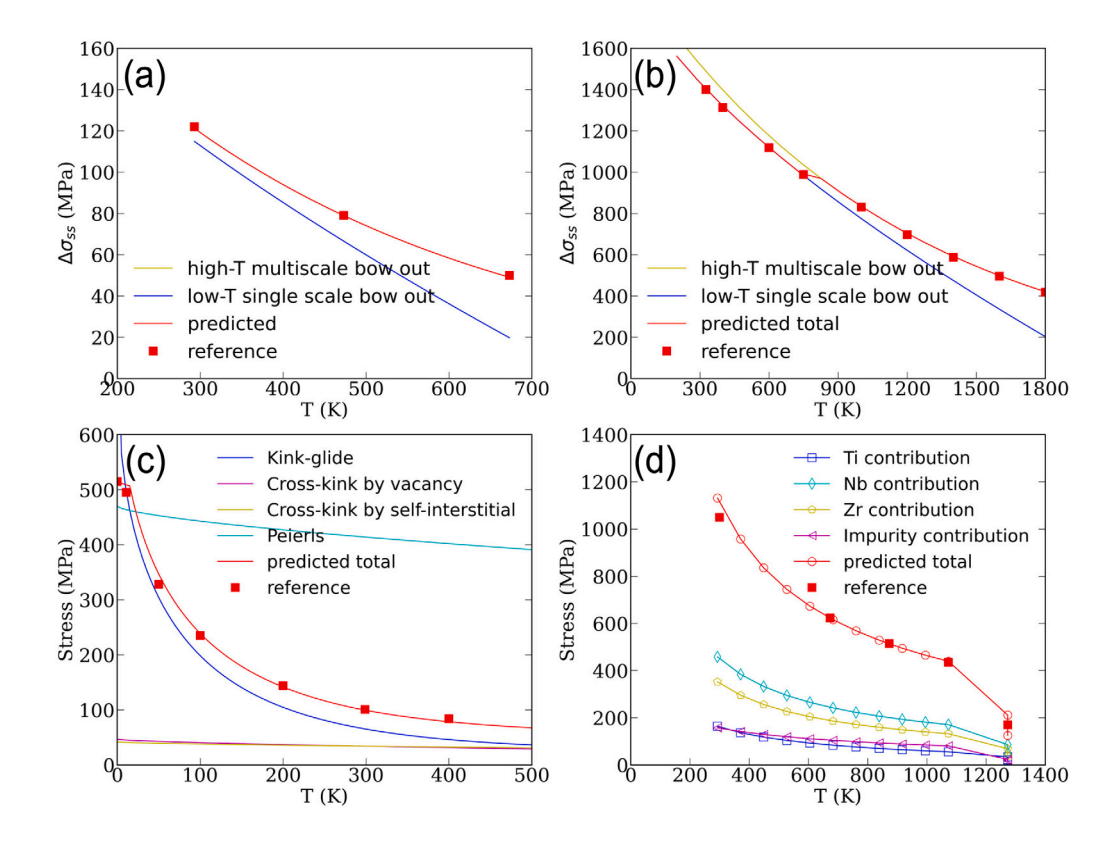


Fig. 2. Predicted temperature-dependent strengths of the selected alloys using the implemented models reproduced by pySSpredict: (a) FCC-edge dislocation model for the CrMnFeCoNi alloy, reference data is from Ref. [19]. (b) BCC-edge dislocation model for the MoNbTaVW alloy, reference data is from Ref. [6]. (c) BCC-screw Curtin model for the Nb95Mo5 alloy, reference data is from Ref. [30].

the calculated Peierls stress using DFT/MD ΔV_p are usually higher than the experimental values. Therefore, the scaling parameters allow users to fit the low-temperature stresses when using properties determined by the DFT/MD simulations. The values in Table 4 were taken from the rescaled quantities in Maresca and Curtin's study. The adjustable kink width, E_k , is set to 10 Burgers vectors by default, a reasonable value for HEAs [16,30].

3.3. BCC screw dislocation — Suzuki model

The TiNbZr equimolar alloy is chosen for presenting the Suzuki model, as seen in Fig. 2(d) for the predicted strengths. The elemental properties are from Rao et al.'s study [30], see Table 5. The Suzuki model decomposes the overall stress into contributions by the solute elements. For example, at room temperature, Nb, Zr, and Ti contribute 458 MPa, 352 MPa, and 164 MPa to the overall strength, respectively. In Rao et al.'s study [30], other interstitial impurities (0.5 at.%) were also considered that an estimated value of 0.5 eV was used for the impurity–screw dislocation interaction, E_{wi} , which further gave rise to about 140 MPa to the predicted strength. In this calculation, the impurity–dislocation interaction contributes to the overall strength by 157 MPa.

In the Suzuki model, Rao et al. proposed that the high-temperature mechanism can be attributed to the jog-dragging mode controlled by the diffusivity of the point defects [30]. The significant drop of stresses from 1073 K to 1273 K is due to the activation of the jog-dragging mode when the condition of $(\sqrt{Dt} > b \text{ with } t = 0.002/\dot{\epsilon})$ is satisfied, see Fig. 2(d). The diffusivity of the alloy is estimated from the reported liquidus temperature $T_l = 1961 \text{ K } [30]$. The liquidus temperature can also be calculated through the implemented function that performs thermodynamic calculations within the TC-Python framework. It can

Table 5Input properties of the BCC TiNbZr equimolar alloy.

Element	a (Å)	E_{wi} (eV)	E_v^f (eV)	E_{si}^f (eV)	μ (GPa)	ν
Nb	3.30	0.054	2.99	5.25	38	0.40
Ti	3.31	-0.028	2.22	2.40	44	0.32
Zr	3.58	-0.053	1.80	3.50	33	0.34
Impurities	-	0.5	-	-	-	-

be seen that the direct usage of the diffusivity data can benefit the Suzuki model by reducing the approximation from liquidus temperatures. The direct computation of the diffusivity can be achieved by the ThermoCalc DICTRA module [27], and the usage and management of the diffusivity data will be implemented in the future version of the code.

The discrepancies between the reference data and the calculated stress can be attributed to (1) the strain rate setting and (2) the numerical error when solving the Eq. (3) set. In Rao et al.'s study, a variation of strain rates between (0.00001/s to 0.01/s) was used. In this paper, the strain rate is 0.001/s for temperatures up to 1073 K. At 1273 K, 0.001/s and 0.0001/s are used in the calculations, corresponding to the upper and lower points in Fig. 2(d). This corresponds to the observation that lower strain rates resulted in lower calculated stresses [30].

The Suzuki model has five parameters to set prior to the stress calculation: the kink width (w_k) , the dislocation density (ρ) , the initial trial values for κ and τ_k , and the exponent for the summation of stress contributions (q). The default values are provided in Table 5 according to Rao et al.'s study for the refractory alloys and user experiences in the minimization process.

4. Solid-solution strength predictions of arbitrary alloys

4.1. Single composition: TiNbZrMo

The BCC TiNbZrMo equimolar alloy is selected to demonstrate the calculations for an arbitrary composition, using the BCC models: BCC-screw-Curtin, BCC-screw-Suzuki, and BCC-edge-Curtin. For the experimental conditions, the stresses are calculated at temperatures ranging from 300 K to 1600 K with the same strain rate of 0.001/s.

For the BCC-screw-Curtin model, a, $\Delta \tilde{E_p}$, ΔV_p , E_k , E_{si}^f , and E_v^f are required. The a, E_{si}^f , and E_v^f of the averaged alloy are calculated by the rule of mixture, using the elemental data in Table 6. The lattice constants are extracted from the experimental measurements of pure metals or binary alloys [36-39], and the point defect formations energies can be obtained from DFT calculations [29]. $\Delta \tilde{E}_{p}$, ΔV_{p} , and E_k have complicated relationship with the composition and alloying components that they require extensive first-principles calculations on dislocation structures [16]. The solute-dislocation energy fluctuation follows a relationship of $\Delta \tilde{E}_p = \sqrt{\sum_n (c_n \Delta \tilde{E}_p(n)^2)}$, where $\Delta \tilde{E}_p(n)$ is the solute-dislocation energy fluctuation due to element-n, and c_n is the concentration of element-n [16]. The $\Delta \tilde{E}_p(n)$ for Nb, Ti, Zr, and Mo in Table 6 are obtained from fitting the $\Delta \tilde{E_p}^r$ values for the NbW, NbMo, and TiNbZr alloys in Maresca and Curtin's study [16]. To validate the fitted values of $\Delta \tilde{E}_p(n)$, the calculated and reported values of $\Delta \tilde{E}_n(n)$ are shown in Fig. 3 with excellent agreement. For E_k , values for Ti33– Nb33-Zr33 and Ti33-Nb17-Zr17 are about 0.25 eV [16]. It is assumed that the E_k for this system is less likely to change, so universal values are assigned to Nb, Ti, and Zr. There is no available E_k data for Mo in the medium of Ti-Nb-Zr alloys; therefore, the E_k for Mo was fitted from the Nb-Mo binary system [16]. For ΔV_p , universal values for Nb, Ti and Zr are obtained from the equimolar Ti33-Nb33-Zr33 alloy, and the data for Mo is obtained from the Nb-Mo binary system [16].

Table 6
Elemental data for Nb, Ti, Zr, and Mo.

Element	a (Å)	E_v^f (eV)	E_{si}^f (eV)	$\Delta \tilde{E_p}(n)~({\rm eV})$	E_k (eV)	ΔV_P (eV/b)	E_{wi} (eV)
Nb	3.30	2.99	5.25	0.0345	0.25	0.01	0.046
Ti	3.31	2.22	2.40	0.0291	0.25	0.01	-0.041
Zr	3.58	1.80	3.50	0.1151	0.25	0.01	-0.101
Mo	3.15	2.74	7.50	0.1579	0.53	0.02	0.070

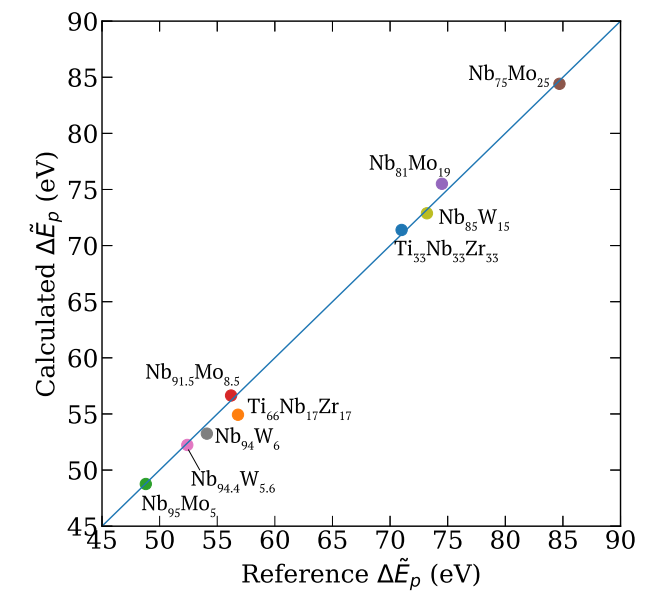


Fig. 3. Solute–dislocation energy fluctuation $(\Delta \tilde{E}_p(n))$ of Ti-Nb-Zr, Nb-W, and Nb–Mo alloys: calculated data vs. reported data in [16].

For the BCC-screw-Suzuki model, a, E_{wi} , E_{si}^f , and E_v^f are required. The values of a, E_{si}^f , and E_v^f are the same as the BCC-screw-Curtin model. The solute–dislocation interaction energies, E_{wi} , are obtained

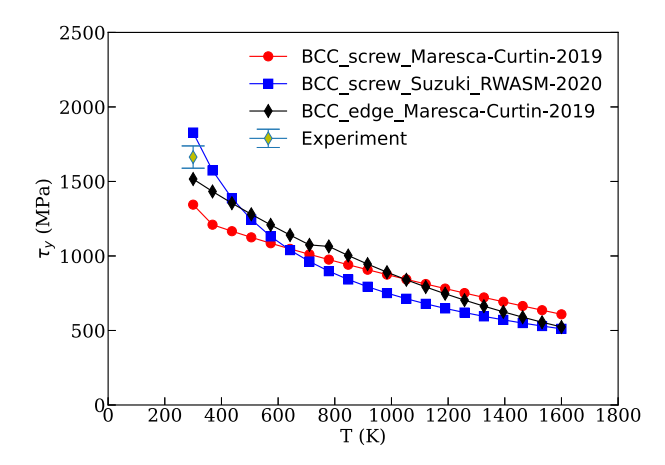


Fig. 4. Temperature dependent of predicted yield stresses for the TiNbZrMo equimolar alloy using three different models. The experimental yield stress at room temperature is obtained from Zhang et al.'s study [41].

from the molecular dynamics simulations in the study from Rao et al. [31]. For the stress minimization processes, the default values of dislocation density, trial κ and τ_{κ} in Table 2 are used.

For the BCC-edge-Curtin model, V_n , and elastic constants are necessary and shown in Table 7. The elastic constants can be calculated with different methods, such as the Vegard's law and the Voigt averaging method [16,19,40]. This example uses the Vegard's law to calculate the shear modulus and Poisson ratio using the elemental data in Table 7. It should be noted that the program also allows users to switch to the Voigt method by setting the set_averaging_scheme ('voigt') and using the 6 \times 6 stiffness matrix instead of shear modulus and Poisson ratio. The α parameter is set to 0.0833 recommended by Maresca et al. [6]; default values of 0.7844 and 7.2993 are used for f_1 and f_2 , respectively.

The temperature-dependent yield stresses predicted by the implemented models are shown in Fig. 4, in which the stresses are multiplied by a Taylor factor of 2.7 for polycrystalline BCC materials in order to compare with the compressive yield strength from experiments [41]. All the considered models predict similar trends of the stresses, which decrease with increasing temperature. Compared to the experimental stress at 300 K, the Suzuki model slightly overestimates the stress while the Curtin-edge and Curtin-screw models slightly underestimate the stress. The variations between the models are within 100 to 200 MPa. especially for the temperatures above 600 K. At higher temperatures, the Curtin models predict higher stresses than the Suzuki model. The comparable values of predicted stresses by different models might suggest that various modes of dislocation motions can compete with one another, depending on the local stresses, dislocation types, and temperature [42-44]. While it is often considered that the mobility of screw dislocations controls the plastic deformation of BCC metals, new evidence by Lee and colleagues showed that contribution from edge dislocations is significant at high temperatures [42]. It is worth mentioning that many BCC RCCAs exhibit stress plateaus from about 600 K to 1000 K [6,11,16,30,45], which may indicate that mechanisms are unclear and not captured in the current models.

4.2. Ternary system: Ti-Nb-Zr

The strengths of ternary and pseudo-ternary alloying systems can be calculated through the ternary_calc_wrapper function. The ternary TiNbZr system is selected to demonstrate the usage of the function. Similar to the single_calc_wrapper, the ternary calculations require the same input structure for the elemental properties. In addition, the ternary calculations require a dictionary-type input containing the elemental symbols, composition ranges, and the increment for creating a evenly-spaced mesh for the ternary diagram.

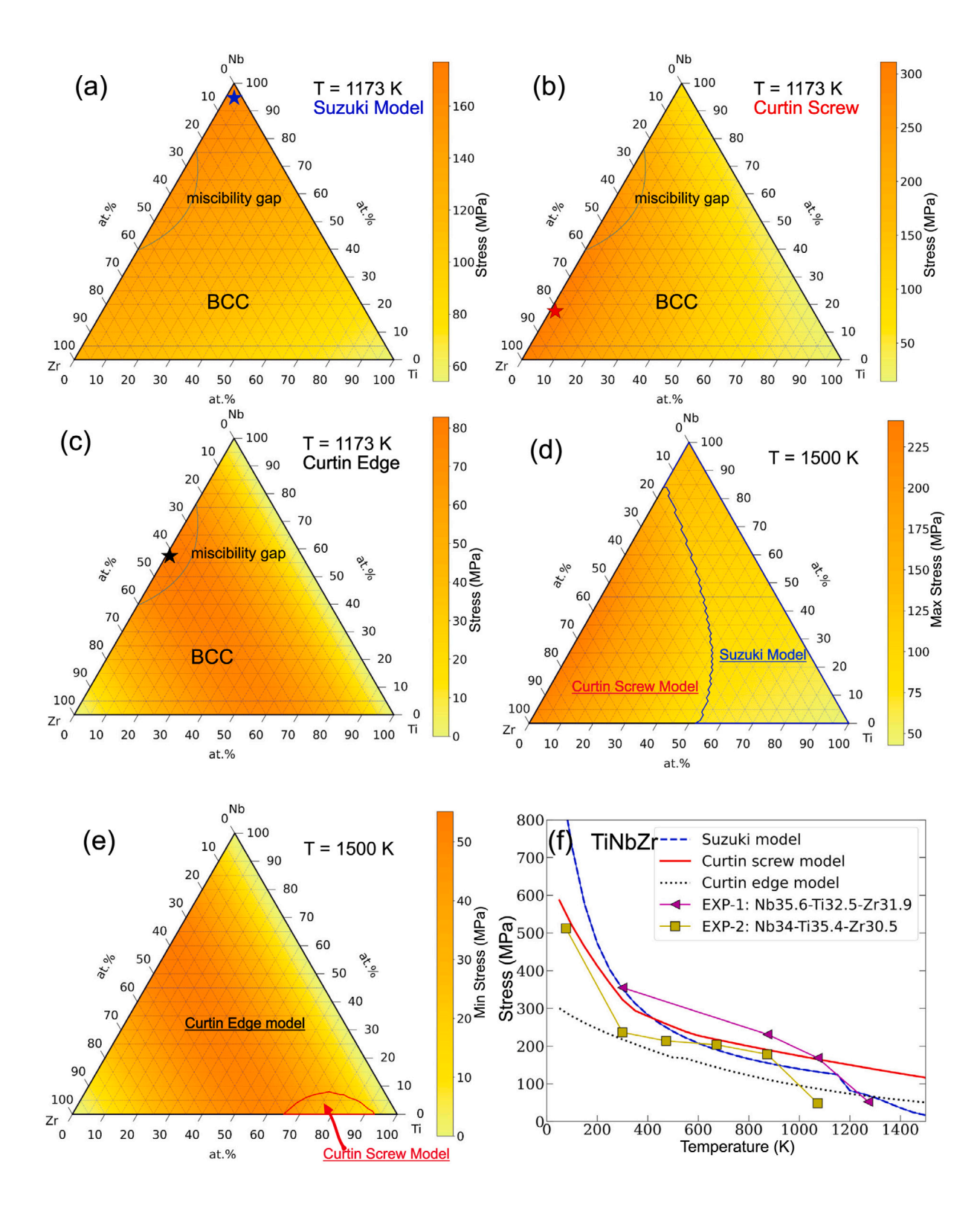


Fig. 5. Strengths of the TiNbZr alloys predicted by different models: (a) Suzuki model at 1173 K, (b) Curtin screw dislocation model at 1173 K, (c) Curtin edge dislocation model at 1173 K. For figure (a)—(c), the predicted ternary isothermal phase diagrams at 1173 K are plotted on top of the stress heatmaps, a large region of BCC single phase and a miscibility gap are shown. (d) The 'mechanism map' predicted at 1500 K, where the heatmap represents the maximum values of the stresses predicted by the models. The left-half of the diagram is contributed by the Suzuki model. (e) The 'mechanism map' at 1500 K, where the heatmap represents the minimum values of the stresses. A large region is contributed by the Suzuki model and the bottom-right area is contributed by the Curtin screw dislocation model. (f) Strengths vs. temperature for the equimolar Ti33Nb33Zr33 alloy. Experimental stresses of alloys with similar compositions are obtained from the studies of Senkov et al. [46] (EXP-1) and Eleti et al. [47] (EXP-2).

For the TiNbZr alloy, several compositions have been studied in [17, 48] while a large area of the ternary space is left unexploited. The strengths of the TiNbZr alloys are predicted using three BCC models: the BCC-screw-Curtin model, the BCC-screw-Suzuki model, and the BCC-edge-Curtin model. The elemental properties for the three different models are provided in Tables 5 and 6. It should be noted that, like other simulation tools, approximations are used in the pySSpredict. For an arbitrary alloy composition, the calculations of different models are discussed in Section 4.1. The elemental data can be found in Tables 5 and 6.

The strengths of the TiNbZr system are calculated and visualized with the ternary phase diagram at 1173 K, see Fig. 5. Three models present different trends of strengthening effects.

For the BCC-screw-Suzuki model, high-strength alloys have higher Nb due to the high Nb-dislocation interaction energy (Fig. 5(a)). For the equimolar TiNbZr alloy, the predicted stress is 122 MPa, slightly lower than the value of 133 MPa extracted from Rao et al.'s study [30]. This is because a dilute concentration of interstitial is considered in their calculations.

For the BCC-screw-Curtin model, high-strength alloys have higher Zr and moderate Nb concentrations (Zr–18Nb), see Fig. 5(b). This is mainly due to the higher $\Delta \tilde{E_p}$ contributed by Zr than by Nb or Ti. The calculated stresses for the equimolar TiNbZr and the Ti-25Nb-25Zr alloys are 153 MPa and 103 MPa, respectively, in good agreement with the values of about 150 MPa and 130 MPa extracted from Maresca and Curtin's study [16], given the fact that the elemental properties are approximated from limited data in this study.

The BCC-edge-Curtin model predicts the stresses based on the elastic interactions between the solute atoms and the stress fields of the dislocations. The maximum strength is observed around the Nb–41Zr alloy, which can be attributed to the large volume misfit and shear modulus predicted at this composition. It is noted that this alloy composition falls inside the miscibility gap of two BCC phases in the phase diagram, see Fig. 5(c). Therefore, it is likely that the experimental yield stress will deviate from the theoretical prediction due to the formation of two phases with different compositions.

Based on the stresses predicted by the models, a 'mechanism map' can be constructed by evaluating the highest/lowest strength at an arbitrary composition. For example, at 1500 K, the heatmaps of Fig. 5(d) and 5(e) represent the highest and the lowest values of stresses, respectively, predicted by the BCC-edge dislocation model, the Suzuki model, and the Curtin screw dislocation model. For the maximum stresses at 1500 K, the left half of Fig. 5(d) is contributed by the Curtin screw dislocation model. The right half of the diagram is contributed by the Suzuki model. For the minimum stresses at 1500 K, the Curtin edge dislocation model is the dominating mechanism, while the Curtin edge dislocation mode contributes to the bottom-right area. It should be noted that the jog-dragging mode is not calculated for the Suzuki model because of a lack of compositionally-dependent diffusivity data.

A comparison of different mechanisms is shown in Fig. 5(f) regarding the temperature-dependent stress of the equimolar TiNbZr. The predicted stresses of the Suzuki model and Curtin screw model are comparable at lower temperatures, while the Suzuki model predicted lower stresses with increasing temperatures. The edge dislocation model predicted the lowest stresses until about 1200 K when the jog-dragging mode of the Suzuki model was activated. For the Ti-33Nb-33Zr, Ti-25Nb-25Zr, and many BCC alloys, it has been found that the plastic deformation is mainly controlled by low-mobility screw dislocations at room temperature [30,48]; however, the high-temperature deformation mechanism remains unclear when the mobilities of the screw and edge components are comparable. As shown in Fig. 5(f), the Curtin screw model significantly overestimates the stresses above 1000 K, which is expected to be controlled by the jog-dragging mode of the Suzuki model. At temperatures above 1200 K, the strength of edge dislocations is becoming more and more important as compared to the screw dislocations predicted by the Suzuki model. It is possible that motions of edge dislocations defeat the screw dislocations to become the major mechanism at higher temperatures for BCC alloys [6,42].

4.3. High-throughput calculations — Refractory alloys

High-throughput calculations of stresses can be achieved by looping over the combinations of alloy systems and compositions using the single_calc_wrapper function. In this demonstration, common refractory CCA elements [11]: Ti, V, Cr, Zr, Nb, Mo, Hf, Ta, and W are selected in the calculation. Al is also included because some Alcontaining RCCAs exhibit higher compressive stress compared to some commercial superalloys [11]. Only the Curtin edge dislocation model is used in the calculations. The strengths of all the ternary, quaternary, and quinary alloy systems with 5 at.% concentration increment are calculated using the elemental properties in Table 7. For the lattice parameters: V, Nb, Mo, Ta, and W are from experimental data [36,37], Ti and Zr are extrapolated from high-T BCC phase data [38,39], Hf is extrapolated from Hf-HEAs data [49], Al is calculated from the DFT atomic radius of FCC Al [25,26], and Cr is extrapolated from Nb-Cr solid solution phase [50]. For the elastic constants, the first-principles elastic constants of the ground-state structures are used [25,26]: Al: FCC phase; Ti, Zr, and Hf: HCP; V, Cr, Nb, Mo, Ta, and W: BCC. Table 7

Lattice parameters, shear moduli and Poisson ratios of the selected elements.

	Ti	V	Cr	Zr	Nb	Mo	Hf	Ta	W	Al
a (Å)	3.31	3.02	3.02	3.58	3.30	3.15	3.65	3.30	3.16	3.22
μ (GPa)	44	46	120	34	38	120	30	69	161	24
ν	0.32	0.36	0.29	0.34	0.40	0.37	0.30	0.34	0.28	0.37

To validate the material inputs, the predicted energy barriers of some RCCAs agree very well with the reported values in Maresca's study [6] (see Fig. 6). It should be noted that the material properties can be slightly different because different data may be used for different alloys in the previous study. [6]. Our calculations calculate the averaged lattice constants and elastic constants via Vegard's law.

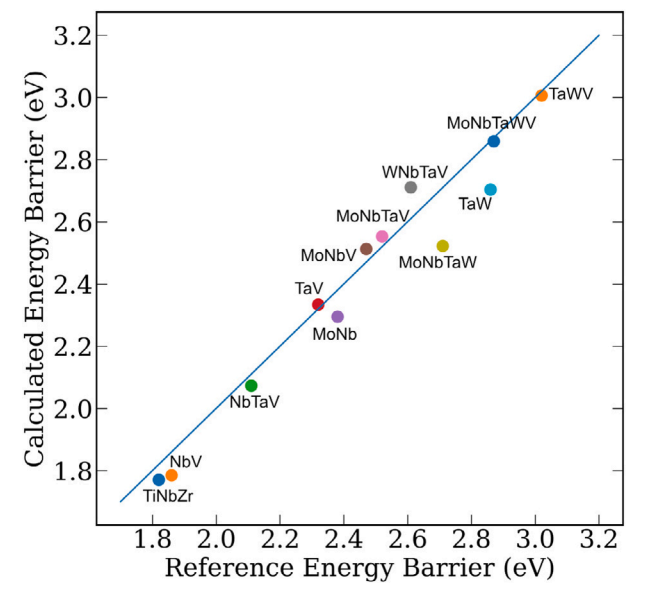


Fig. 6. Energy barriers of some refractory alloys calculated by this study compared to the reference data [6].

The workflow shown in Fig. 7 was used to perform high-throughput calculations of thermodynamic phase stability and solid-solution strengths of quaternary RCCAs. With a composition increment of 5 at.%, 203,490 compositions were generated. For arbitrary quaternary RCCAs at 1500 K, thermodynamically-stable phases were predicted by TC-Python with the TCHEA4 database (see Fig. 7). 61,049 alloys were predicted to maintain single BCC solid-solution phase at 1500 K and were augmented to solid-solution stress calculations using the main functions in pySSpredict. For these 61,049 alloys, we rank the elements by the number of alloys containing them: Ti (36,422) > Nb (34,675) > V (33,437) > Mo (29,439) > Ta (25,723) > W (20,825) > Hf (19,486)

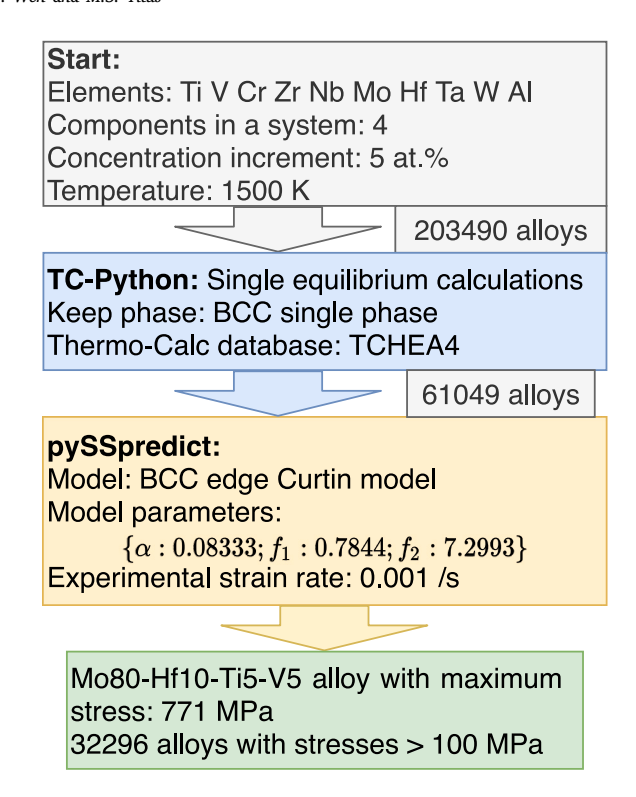


Fig. 7. Workflow for high-throughput calculations of phase stability and solid-solution strengths for quaternary RCCAs.

> Cr (15,468) > Zr (14,693) > Al (14,028). Based on the ranking, Ti, Nb, V, and Mo are more likely to form BCC alloys while Hf, Cr, Zr, and Al can form secondary phases. For the predicted BCC alloys, solidsolution strengths were predicted using the BCC-edge-Curtin model. 32,296 alloys exhibit yield stresses higher than 100 MPa at 1500 K. Fig. 8 reports 50 alloys with the highest strengths from 640 MPa to 771 MPa. Within the edge dislocation model, large atomic misfits of the atoms in the averaged matrix result in higher athermal yield stresses and energy barriers [6,15]. For example, the energy barriers of the MoNbTaWV and TaWV alloys are larger than 2.9 eV, as seen in Fig. 2, leading to excellent compressive strengths above 1500 K [51]. Lee et al. predicted the strengths for more than 10 million RCCAs and found that more than 1 million compositions have yield stresses higher than 2 GPa at 1300 K [42], while the phase information is missing for experimental design. The reported alloys in Fig. 8 are worth further investigation for studying the strengthening mechanisms and validation.

For alloy design, screw dislocation mechanisms should also be considered for constructing the 'mechanism maps'. However, the scarce data of solute–screw dislocation interactions has yet to satisfy the demand for high-throughput calculations, mainly due to the complicated and time-consuming first-principles calculations of these properties. Combining the stress predictions with other properties, such as the oxidation resistance and ductility, provides a road map for materials selections to facilitate the experimental fabrications and measurements. All the input and predicted data for the 61,049 RCCAs are included in the Github code repository [22].

5. Conclusions

We developed an open-source python-based toolkit for solid solution strengthening calculations and implemented the latest models for multi-component alloys. We demonstrate the major functions of the program by coupling the stress predictions, thermodynamic calculations, high-throughput calculations, and visualization functions. We reinvestigate the already-explored CrMnFeCoNi, MoNbTaVW,

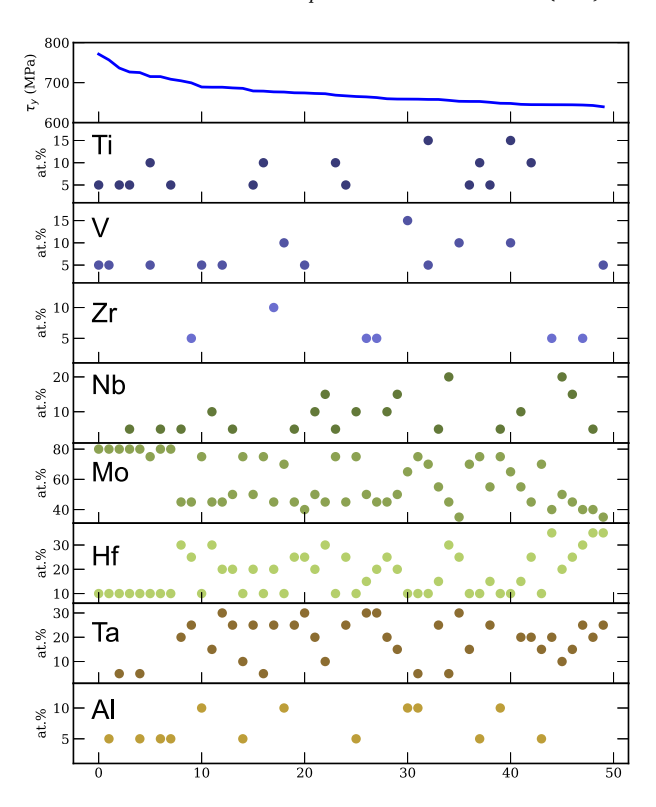


Fig. 8. Curtin edge model predicted strengths at 1500 K vs. alloy compositions for the top-50 alloys with the high stresses. All the alloys are predicted to maintain single BCC solid-solution phase at 1500 K. TCHEA4 database was used in the TC-Python phase calculations.

Nb95Mo5, and TiNbZr alloys to show the stress contributions of various mechanisms. We discover that there can be competing strengthening mechanisms for the TiNbZr ternary alloys at various temperatures and compositions through the 'mechanism map' of different strengthening models. The 'mechanism map' can be generally applied to other systems to design new structural alloys. And finally, the high-throughput calculations of the refractory CCAs can be used to guide the experimental synthesis of new alloys with broader ranges of properties.

CRediT authorship contribution statement

Dongsheng Wen: Conceptualization, Methodology, Validation, Visualization, Data curation, Writing – original draft, Writing – review & editing. **Michael S. Titus:** Conceptualization, Methodology, Software, Resources, Writing – review & editing, Supervision, Project administration, Funding acquisition.

Declaration of competing interest

The authors declare that they have no known competing financial interests or personal relationships that could have appeared to influence the work reported in this paper.

Data availability

pySSpredict is an open-source Python package and is available to download at https://github.com/Dongsheng-Wen/pySSpredict. Demonstration codes can be run in the cloud on nanoHUB at https://nanohub.org/tools/pysspredict. For the high-throughput calculations of RCCAs, the input and predicted data is shared in the supplementary documents.

Acknowledgments

This material is based upon work supported by the National Science Foundation, United States under Grant No. (CAREER DMR-1848128). The authors would additionally like to acknowledge Purdue University for supporting this work through start-up funds. This research was supported in part through computational resources provided by Information Technology at Purdue, West Lafayette, Indiana [52].

References

- R.O. Ritchie, The conflicts between strength and toughness, Nature Materials 10 (11) (2011) 817–822.
- [2] A. Lisovsky, N. Tkachenko, V. Kebko, Structure of a binding phase in re-alloyed WC-Co cemented carbides, International Journal of Refractory Metals and Hard 414 Materials 10 (1) (1991) 33–36.
- [3] E. Almond, B. Roebuck, Identification of optimum binder phase compositions for improved wc hard metals, Materials Science and Engineering: A 105 (1988) 237–248.
- [4] R.C. Reed, The Superalloys: Fundamentals and Applications, Cambridge University Press, 2008.
- [5] C. Slone, J. Miao, E. George, M.J. Mills, Achieving ultra-high strength and ductility in equiatomic CrCoNi with partially recrystallized microstructures, Acta Materialia 165 (2019) 496–507.
- [6] F. Maresca, W.A. Curtin, Mechanistic origin of high strength in refractory BCC high entropy alloys up to 1900K, Acta Materialia 182 (2020) 235–249.
- [7] Z. He, N. Jia, D. Ma, H.-L. Yan, Z. Li, D. Raabe, Joint contribution of transformation and twinning to the high strength-ductility combination of a FeMnCoCr high entropy alloy at cryogenic temperatures, Materials Science and Engineering: A 759 (2019) 437–447.
- [8] J.-W. Yeh, S.-K. Chen, S.-J. Lin, J.-Y. Gan, T.-S. Chin, T.-T. Shun, C.-H. Tsau, S.-Y. Chang, Nanostructured high-entropy alloys with multiple principal elements: novel alloy design concepts and outcomes, Advanced engineering materials 6 (5) (2004) 299–303.
- [9] B. Cantor, I. Chang, P. Knight, A. Vincent, Microstructural development in equiatomic multicomponent alloys, Materials Science and Engineering: A 375 (2004) 213–218.
- [10] E.P. George, D. Raabe, R.O. Ritchie, High-entropy alloys, Nature Review Materials 4 (8) (2019) 515–534.
- [11] D.B. Miracle, O.N. Senkov, A critical review of high entropy alloys and related concepts, Acta Materialia 122 (2017) 448–511, http://dx.doi.org/10.1016/j. actamat.2016.08.081.
- [12] C.B. Finfrock, A.J. Clarke, G.A. Thomas, K.D. Clarke, Austenite stability and strain hardening in c-mn-si quenching and partitioning steels, Metallurgical and Materials Transactions A 51 (5) (2020) 2025–2034.
- [13] E.P. George, W. Curtin, C.C. Tasan, High entropy alloys: A focused review of mechanical properties and deformation mechanisms, Acta Materialia 188 (2020) 425, 474
- [14] R. Labusch, A statistical theory of solid solution hardening, Physica Status Solidi (b) 41 (2) (1970) 659–669.
- [15] C. Varvenne, A. Luque, W.A. Curtin, Theory of strengthening in fcc high entropy alloys, Acta Materialia 118 (2016) 164–176.
- [16] F. Maresca, W.A. Curtin, Theory of screw dislocation strengthening in random BCC alloys from dilute to 'High-Entropy' alloys, Acta Materialia 182 (2020) 144–162.
- [17] S. Rao, B. Akdim, E. Antillon, C. Woodward, T. Parthasarathy, O.N. Senkov, Modeling solution hardening in BCC refractory complex concentrated alloys: NbTiZr, Nb1. 5TiZr0. 5 and Nb0. 5TiZr1. 5, Acta Materialia 168 (2019) 222–236.
- [18] C. Varvenne, W.A. Curtin, Predicting yield strengths of noble metal high entropy alloys, Scripta Materialia 142 (2018) 92–95.
- [19] C. Varvenne, G.P.M. Leyson, M. Ghazisaeidi, W.A. Curtin, Solute strengthening in random alloys, Acta Materialia 124 (2017) 660–683.
- [20] F.G. Coury, K.D. Clarke, C.S. Kiminami, M.J. Kaufman, A.J. Clarke, High throughput discovery and design of strong multicomponent metallic solid solutions, Scientific Reports 8 (1) (2018) 1–10.
- [21] D. Wen, C.-H. Chang, S. Matsunaga, G. Park, L. Ecker, S.K. Gill, M. Topsakal, M.A. Okuniewski, S. Antonov, D.R. Johnson, et al., Structure and tensile properties of Mx (MnFeCoNi) 100-x solid solution strengthened high entropy alloys, Materialia 9 (2020) 100539.
- [22] D. Wen, M. Titus, pySSpredict: A python-based tool for predicting solid-solution strengthening, URL https://github.com/Dongsheng-Wen/pySSpredict.
- [23] D. Wen, M. Titus, Python-based Toolkit for Solid Solution Strengthening Prediction, URL https://nanohub.org/resources/pysspredict.

- [24] W. McKinney, Data structures for statistical computing in python, in: S. van der Walt, J. Millman (Eds.), Proceedings of the 9th Python in Science Conference, 2010. pp. 56–61. http://dx.doi.org/10.25080/Majora-92bf1922-00a.
- [25] A. Jain, S.P. Ong, G. Hautier, W. Chen, W.D. Richards, S. Dacek, S. Cholia, D. Gunter, D. Skinner, G. Ceder, K.a. Persson, The Materials Project: A materials genome approach to accelerating materials innovation, APL Materials 1 (1) (2013) 011002, http://dx.doi.org/10.1063/1.4812323, URL http://link.aip.org/link/AMPADS/v1/i1/p011002/s1&Agg=doi.
- [26] A. Jain, S.P. Ong, G. Hautier, W. Chen, W.D. Richards, S. Dacek, S. Cholia, D. Gunter, D. Skinner, G. Ceder, et al., Commentary: The materials project: A materials genome approach to accelerating materials innovation, APL Materials 1 (1) (2013) 011002.
- [27] J.-O. Andersson, T. Helander, L. Höglund, P. Shi, B. Sundman, Thermo-Calc & DICTRA, computational tools for materials science, Calphad 26 (2) (2002) 273–312.
- [28] S.T. Reeve, A. Strachan, Functional uncertainty quantification for isobaric molecular dynamics simulations and defect formation energies, Modelling and Simulation in Materials Science and Engineering 27 (4) (2019) 044002.
- [29] B. Medasani, M. Haranczyk, A. Canning, M. Asta, Vacancy formation energies in metals: A comparison of MetaGGA with LDA and GGA exchange-correlation functionals, Computational Materials Science 101 (2015) 96–107.
- [30] S. Rao, C. Woodward, B. Akdim, O.N. Senkov, D.B. Miracle, Theory of solid solution strengthening of BCC chemically complex alloys, Acta Materialia 209 (2021) 116758.
- [31] S. Rao, E. Antillon, C. Woodward, B. Akdim, T. Parthasarathy, O. Senkov, Solution hardening in body-centered cubic quaternary alloys interpreted using Suzuki's kink-solute interaction model, Scripta Materialia 165 (2019) 103–106.
- [32] G.P.M. Leyson, L. Hector Jr., W.A. Curtin, Solute strengthening from first principles and application to aluminum alloys, Acta Materialia 60 (9) (2012) 3873–3884.
- [33] S. Nag, W.A. Curtin, Effect of solute-solute interactions on strengthening of random alloys from dilute to high entropy alloys (vol 200, pg 659, 2020), Acta Materialia 204 (ARTICLE) (2021) 116439.
- [34] A. Ghafarollahi, F. Maresca, W. Curtin, Solute/screw dislocation interaction energy parameter for strengthening in bcc dilute to high entropy alloys, Modelling and Simulation in Materials Science and Engineering 27 (8) (2019) 085011.
- [35] D. Ma, M. Friák, J. von Pezold, D. Raabe, J. Neugebauer, Computationally efficient and quantitatively accurate multiscale simulation of solid-solution strengthening by ab initio calculation, Acta Materialia 85 (2015) 53–66.
- [36] G. Simmons, Single crystal elastic constants and calculated aggregate properties, Tech. rep., Southern Methodist Univ Dallas Tex, 1965.
- [37] B. Yin, F. Maresca, W.A. Curtin, Vanadium is an optimal element for strengthening in both fcc and bcc high-entropy alloys, Acta Materialia 188 (2020) 486–491.
- [38] W. Petry, A. Heiming, J. Trampenau, M. Alba, C. Herzig, H. Schober, G. Vogl, Phonon dispersion of the bcc phase of group-IV metals. I. bcc titanium, Physical Review B 43 (13) (1991) 10933.
- [39] A. Heiming, W. Petry, J. Trampenau, M. Alba, C. Herzig, H. Schober, G. Vogl, Phonon dispersion of the bcc phase of group-IV metals. II. bcc zirconium, a model case of dynamical precursors of martensitic transitions, Physical Review B 43 (13) (1991) 10948.
- [40] S. Nag, C. Varvenne, W.A. Curtin, Solute-strengthening in elastically anisotropic fcc alloys, Modelling and Simulation in Materials Science and Engineering 28 (2) (2020) 025007
- [41] Y. Zhang, X. Yang, P. Liaw, Alloy design and properties optimization of high-entropy alloys, JOM 64 (7) (2012) 830–838.
- [42] C. Lee, F. Maresca, R. Feng, Y. Chou, T. Ungar, M. Widom, K. An, J.D. Poplawsky, Y.-C. Chou, P.K. Liaw, et al., Strength can be controlled by edge dislocations in refractory high-entropy alloys, Nature Communications 12 (1) (2021) 1–8.
- [43] D. Caillard, Kinetics of dislocations in pure Fe. Part I. In situ straining experiments at room temperature, Acta Materialia 58 (9) (2010) 3493–3503.
- [44] D. Caillard, Kinetics of dislocations in pure Fe. Part II. In situ straining experiments at low temperature, Acta Materialia 58 (9) (2010) 3504–3515.
- [45] O.N. Senkov, D.B. Miracle, K.J. Chaput, J.-P. Couzinie, Development and exploration of refractory high entropy alloys—A review, Journal of Materials Research 33 (19) (2018) 3092–3128.
- [46] O. Senkov, S. Rao, K. Chaput, C. Woodward, Compositional effect on microstructure and properties of NbTiZr-based complex concentrated alloys, Acta Materialia 151 (2018) 201–215.
- [47] R.R. Eleti, N. Stepanov, N. Yurchenko, S. Zherebtsov, F. Maresca, Cross-kink unpinning controls the medium-to high-temperature strength of body-centered cubic NbTiZr medium-entropy alloy, Scripta Materialia 209 (2022) 114367.

- [48] F. Mompiou, D. Tingaud, Y. Chang, B. Gault, G. Dirras, Conventional vs harmonic-structured β-Ti-25Nb-25Zr alloys: A comparative study of deformation mechanisms, Acta Materialia 161 (2018) 420–430.
- [49] J.-P. Couzinié, L. Lilensten, Y. Champion, G. Dirras, L. Perrière, I. Guillot, On the room temperature deformation mechanisms of a TiZrHfNbTa refractory high-entropy alloy, Materials Science and Engineering: A 645 (2015) 255–263.
- [50] D. Thoma, J. Perepezko, An experimental evaluation of the phase relationships and solubilities in the Nb-Cr system, Materials Science and Engineering: A 156 (1) (1992) 97–108.
- [51] O.N. Senkov, G.B. Wilks, J.M. Scott, D.B. Miracle, Mechanical properties of Nb25Mo25Ta25W25 and V20Nb20Mo20Ta20W20 refractory high entropy alloys, Intermetallics 19 (5) (2011) 698–706.
- [52] G. McCartney, T. Hacker, B. Yang, Empowering faculty: A campus cyberinfrastructure strategy for research communities, Educause Review (2014) URL https://er.educause.edu/articles/2014/7/empowering-faculty-acampus-cyberinfrastructure-strategy-for-research-communities.